Bioinspired synthesis of self-assembled calcium phosphate nanocomposites using block copolymer-peptide conjugates

Yusuf Yusufoglu,[a] Yanyan Hu,[a] Mathumai Kanapathipillai, Matthew Kramer, and Yunus E. Kalay
Ames Laboratory, Ames, Iowa 50011

P. Thiyagarajan
Advanced Photon Source, Argonne National Laboratory, Argonne, Illinois 60439

Mufit Akinc, Klaus Schmidt-Rohr, and Surya Mallapragada[b]
Ames Laboratory, Ames, Iowa 50011

(Received 29 April 2008; accepted 18 August 2008)

Thermoreversibly gelling block copolymers conjugated to hydroxyapatite-nucleating peptides were used to template the growth of inorganic calcium phosphate in aqueous solutions. Nuclear magnetic resonance (NMR), Fourier transform infrared (FTIR), transmission electron microscopy, x-ray diffraction, and small-angle scattering were used to characterize these samples and confirm that the peptides promoted the growth of hydroxyapatite as the inorganic phase. Three different polymer templates were used with varying charges on the polymer chains (nonionic, anionic, and zwitterionic), to investigate the role of charge on mineralization. All of the polymer-inorganic solutions exhibited thermoreversible gelation above room temperature. Nanocomposite formation was confirmed by solid-state NMR, and several methods identified the inorganic component as hydroxyapatite. Small angle x-ray scattering and electron microscopy showed thin, elongated crystallites. Thermogravimetric analysis showed an inorganic content of 30–45 wt% (based on the mass of the dried gel at ~200 °C) in the various samples. Our work offers routes for bioinspired bottom-up approaches for the development of novel, self-assembling, injectable nanocomposite biomaterials for potential orthopedic applications.

I. INTRODUCTION

Tremendous literature has appeared in recent years to explore ways to mimic biomineralization[1–4] and to understand the mechanism(s) involved in it with proteins, enzymatic biocatalysts, and other biopolymers.[5–9] Numerous studies have appeared on the in vitro synthesis and characterization of biominerals including calcium phosphate, calcium carbonate, and silica.[10–15] All of these studies have focused on templating at the nanoscale or at the macroscale, but mostly only on the surface.

Controlling the structure at the molecular level as well as impressing hierarchical order over multiple-length scales as seen commonly in nature is a formidable challenge that has not been achieved yet, but significant progress is being made in these directions. Polymer templating has the advantage of molecular-level control and a promise to extend to the macroscale by hierarchical ordering. Our recent work has shown that synthetic block copolymers that undergo self-assembly at multiple-length scales can serve as effective templates for precipitation of calcium phosphates on nanoscale micelles, which can self-assemble further into macroscale gels and solids.[16] This is one of the first approaches for bottom-up design of macroscale composites with hierarchical order down to the nanoscale completely by self-assembly. However, the use of polymer templates alone does not provide biological specificity for controlled growth of the inorganic phase. Therefore, here we report the synthesis of thermoreversibly self-assembling polymer templates with attached hydroxyapatite-nucleating peptides,[17] which were used to control the biomineralization process and to form polymer-hydroxyapatite nanocomposites completely by self-assembly. These novel systems that transition from liquid to solid at physiological temperatures could form the basis for injectable nanocomposites for orthopedic repair, such as in bone or cartilage defects. This allows them to conform to the shape of the defect and form solids at physiological temperatures. Characterization of the nanostructure and composition of the bioinspired nanocomposites remains a challenge. We report the use of a variety of complementary techniques including solid-state nuclear magnetic resonance (NMR), small-angle scattering, and

[a]These authors contributed equally to this work.
[b]Address all correspondence to this author.
e-mail: suryakm@iastate.edu
DOI: 10.1557/JMR.2008.0388

transmission electron microscopy to elucidate the structure and composition of these bioinspired materials.

II. MATERIALS AND METHODS

The hydroxyapatite-nucleating peptide (DSKSDSSKSESDSS), with a molecular weight of 1445 Da and theoretical pI of 4.23, was synthesized by Genscript Corporation (Piscataway, NJ), with a purity of ~95% and used as obtained. All other materials used were obtained from either Sigma-Aldrich (St. Louis, MO) or Fisher Scientific (Fairlawn, NJ) and were of high purity.

III. SYNTHESIS AND CHARACTERIZATION OF BLOCK COPOLYMERS AND THEIR CONJUGATES

A. Polymer synthesis method and scheme

Pluronic F127 [poly(ethyelene oxide)-*b*-poly(propylene oxide)-*b*-poly(ethylene oxide)] with a molecular weight of 12,600 (BASF Corp., Florham Park, NJ) was used to synthesize Pluronic-based anionic (PentaPAA) (M_n = 17,458, PDI 1.14) and zwitterionic (PentaPZ) (M_n = 15,100, PDI 1.17) pentablock copolymers using an atom transfer radical polymerization (ATRP) technique as previously reported.[18,19] These polymers are shown in Scheme 1. The Pluronic and PentaPZ end groups were modified to obtain carboxyl end groups as described below. The Pluronic and the two pentablock copolymers were then conjugated with the hydroxyapatite binding peptide using *N*-hydroxyl succinimide (NHS) chemistry.[20,21] The peptide copolymer conjugation schemes used are shown below.

Pluronic F127

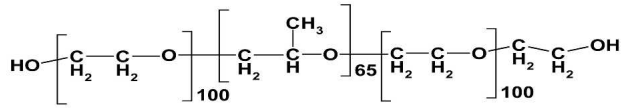

PentaPZ

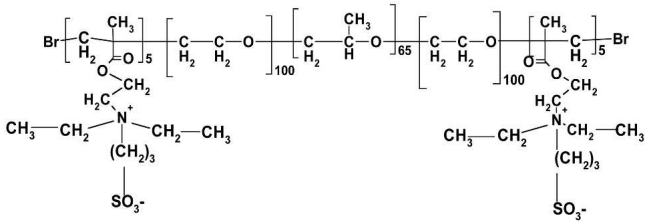

PentaPAA

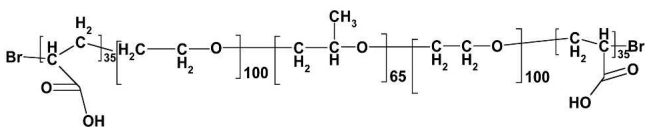

SCHEME 1. Block copolymer structures.

B. Pluronic end group modification (Scheme 2)

The hydroxyl end groups of Pluronic were converted to carboxyl groups by treating with succinic anhydride in pyridine as reported in the literature.[22] In short, Pluronic (32 g, 2.5 mmol) and succinic anhydride (1 g, 10 mmol) were dissolved in pyridine (100 mL), and the reaction was carried out at 40 °C for 24 h. The mixture was then precipitated in diethyl ether, dissolved in toluene, and reprecipitated in diethyl ether. The product was then dried under vacuum.

C. PentaPZ end group modification (Scheme 3)

The transformation of bromine end functional PentaPZ into azide end-functional PentaPZ was adopted from literature.[23] In short, the bromine end functionalized pentablock (15,100 g mol^{-1}, 5.4 g, 0.36 mmol), sodium azide (234 mg, 3.6 mmol), and dimethyl formamide (15 mL) were added in a flask and stirred well. The mixture was reacted for 24 h at 50 °C. After that, the azide-functionalized pentablock was precipitated in *n*-hexane, filtered, and dried under reduced pressure. Click coupling was used to convert the azide end-functionalized PentaPZ to the carboxyl-functionalized end group as reported previously in literature.[20,23] In a round-bottom flask, azide-functionalized PentaPZ (1.65 g, 0.11 mmol), copper bromide (47 mg, 0.33 mmol), and Nppm-ligand (99 mg, 0.66 mmol) were added. After capping the flask with a septum, the mixture was purged with argon for a couple of minutes. Degassed THF (4 mL) was then added into the mixture. Pentynoic acid (64.8 mg, 0.66 mmol) was added through a microsyringe. The mixture was then stirred overnight at room temperature. The carboxyl-functionalized PentaPZ was precipitated in *n*-hexane, filtered, and dried under vacuum.

D. Polymer-peptide conjugate synthesis (Scheme 4)

The carboxyl-terminated Pluronic or PentaPZ, or the acrylic groups of PentaPAA polymers, were esterified with NHS as reported in literature.[21] To a round-bottom flask connected with an argon line and bubbler, Pluronic/PentaPZ/PentaPAA (0.128 mmol), 0.0792 g of *N*,*N*′-dicyclohexylcarbodiimide (3 × excess, 0.384 mol), 0.0442 g of NHS (3 × excess, 0.384 mol), and 8 mL of

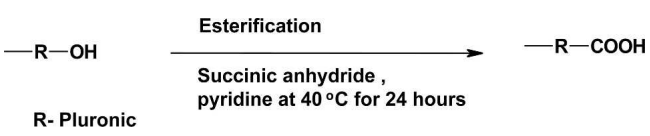

SCHEME 2. Pluronic end group modification.

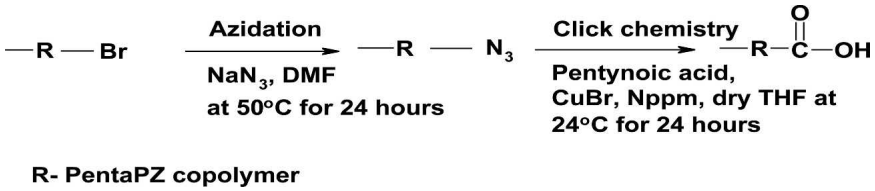

SCHEME 3. PentaPZ end group modification.

a. NHS chemistry on carboxyl endgroups of Pluronic and PentaPZ

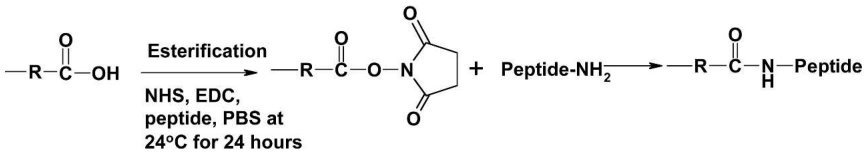

b. NHS chemistry on acrylic acid groups of PentaPAA

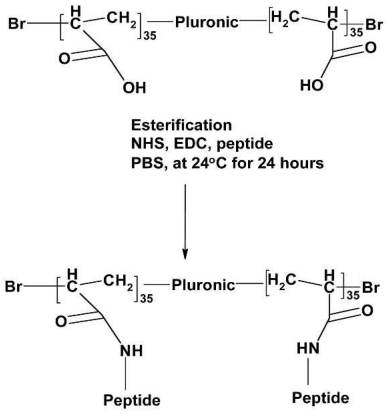

Note: Here peptides were attached randomly to acrylic acid groups.
Only few acrylic acids blocks were conjugated with peptides.

SCHEME 4. Pluronic and Pentablock copolymers peptide conjugation a. NHS chemistry on carboxyl end groups of Pluronic and PentaPZ.

dichloromethane were added. The reaction was carried out at room temperature for 24 h. The reaction mixture was then filtered and precipitated in cold diethyl ether. The NHS attachment was verified by ^{1}H NMR with ester peak at approximately ~2.7 ppm.

The NHS-functionalized polymer was then conjugated with the hydroxyapatite binding peptide as described in the literature.[21] NHS polymer (1.5 g) was added to a solution of 12 mg of peptide in 50 mL of PBS (pH 7.4) with stirring at room temperature. After 4 h, an additional 1.5 g of NHS-polymer was added to the mixture. The reaction was maintained at room temperature for 24 h. A small amount of the reacted mixture was then lyophilized, and the conjugation efficiency was determined using reverse-phase, high-pressure liquid chromatography (RP-HPLC). The rest of the reaction mixture was dialyzed against water using a cellulose ester membrane with a molecular weight cutoff of 3500 (Spectrum Labs, Rancho Dominguez, CA) for 48 h to remove the uncoupled peptide. The polymer-peptide solution was then lyophilized, a pure white powder was obtained, and the peptide attachment was then qualitatively characterized with ^{1}H NMR.

The thermoreversible gelation behavior of the polymers was studied by simple gel inversion. A gradient RP-HPLC method was used to measure the conjugation efficiency of the peptide to the polymer. A Shimadzu C-18 analytical column (5 μm, 4.6 × 250 mm) was used. A flow rate of 1 mL/min was used for the gradient elution with the mobile phases of 0.05% TFA in acetonitrile (solution A) and 0.065% TFA in 100% water (solution B). The mobile phase was run as follows: (i) 5% A for the first 0.01 min; (ii) 25% for the next 24.99 min; and (iii) 100% A for the last 5 min (total run 30 min). The polymer-peptide conjugate was injected into the system, and the unreacted peptide was detected using the UV detector at 220 nm. The concentrations of the unreacted peptide were then calculated using the calibration curve

obtained for the pure peptide using the same method. Amount of conjugated peptide was then found by subtracting the unreacted peptide from the initial added peptide to the polymer-peptide conjugation reaction.

E. Block copolymer: Calcium phosphate nanocomposite synthesis

The following procedure was used to obtain calcium phosphate (CaP)-block copolymer nanocomposite hydrogel samples: 1.2 g of copolymer-peptide conjugate obtained by attaching peptide blocks to Pluronic F127 (designated as Pluronic-Pep) and 1.2 g of pure Pluronic F127 were mixed with 5.0 mL of $Ca(Cl)_2$ solution (4.0 M). The calcium containing polymer-peptide solution was kept in a refrigerator (at T≈1 °C) for 2 days. Then, 3.0 mL of $(NH_4)_2HPO_4$ solution (4.0 M) was added and kept in the refrigerator for another 2 days before aging at room temperature for 2 days to form a hydrogel nanocomposite containing approximately 22 wt% polymer-peptide. The pH of the hydrogel sample was maintained at ~8 by adding 6 M NaOH solution. The sample is referred to as Pluronic-Pep22-8, where the numbers 22 and 8 refer to wt% of the polymer-peptide conjugate and pH of the gel, respectively.

To prepare other CaP/hydrogel samples, a similar procedure was followed using appropriate amounts of triblock Pluronic F127, PentaPAA, and PentaPZ with peptide groups attached (designated as Pluronic, PentaPAA-Pep, and PentaPZ-Pep, respectively). Finally, Pluronic30-8, PentaPAA-Pep30-8 and PentaPZ-Pep45-8 hydrogel samples were prepared, where the first (30, 30, and 45) and second numbers (8) refer to polymer content and pH of the gel, respectively. In addition, hydroxyapatite (HAp) precipitated from an aqueous solution of $Ca(Cl)_2$ and $(NH_4)_2HPO_4$ at pH ~8, and polymer hydrogels prepared in deionized water were used as the control solutions in the present study. The formation of HAp in CaP/polymer hydrogels is believed to take place along the following chemical reaction:

$$10Ca(Cl)_2 + 6(NH_4)_2HPO_4 + 2H_2O \rightarrow Ca_{10}(PO_4)_6(OH)_2 + 12(NH_4)Cl + 8HCl \quad .$$

F. Characterization

Calcium phosphate nanocomposite samples were analyzed by various characterization methods: x-ray diffraction (XRD), Fourier transform infrared spectroscopy (FTIR), thermogravimetric analysis (TGA), bright-field (BF) transmission electron microscopy (TEM), scanning TEM (STEM) using a high-angle annular dark-field (HAADF) detector, high-resolution TEM (HRTEM), and selected-area electron diffraction (SAED). Moreover, the atomic Ca/P ratio was also monitored by energy-dispersive spectroscopy (EDS) in the STEM-EDX.

The phase composition and crystallinity of the samples were assessed by using a theta-theta x-ray diffractometer (XDS-2000; Scintag, Cupertino, CA) and operating at 45 kV and 40 mA. The scanning rate was 0.60°/min, with a sampling interval of 0.02° over a range of $10° \leqslant 2\theta \leqslant 60°$. To minimize drying, hydrogel XRD samples were analyzed immediately following preparation. Scintag DMSNT search/match software and the ICDD 2007 database were used for the phase analysis. FTIR spectra were recorded with a Bruker spectrometer (Bruker IFS-66v; Bruker Optics Inc., Billerica, MA) over 400–4000 cm^{-1} with a 4 cm^{-1} resolution and averaging 32 scans. For the FTIR analysis, vacuum-dried samples were pressed into KBr pellets containing approximately 1 wt% sample. The content of inorganic phase (HAp) in the nanocomposites was estimated from TGA performed with a PerkinElmer thermo gravimetric analyzer (TGA 7; PerkinElmer, Downers Grove, IL). Approximately 60 mg of the gel sample was heated in flowing air. The sample was heated to 50 °C, held at this temperature for 1 min, then ramped to 120 °C at a rate of 5.00 °C/min, and to 600 °C at a rate of 10.00 °C/min.

G. Solid-state NMR

Solid-state NMR experiments were performed using a Bruker DSX400 spectrometer (Bruker-Biospin, Rheinstetten, Germany) at 400 MHz for ^1H and 162 MHz for ^{31}P. A Bruker 4-mm double resonance magic-angle spinning (MAS) probehead was used for 6.5-kHz and 7-kHz MAS ^{31}P or ^1H–^{31}P experiments. The 90° pulse lengths were 5 μs for ^1H and 4 μs for ^{31}P. The direct-polarization experiments were carried out with recycle delays of 100 s at 7 kHz MAS. The 2D ^1H-^{31}P correlation experiments without homonuclear decoupling, using the wide-line separation (WISE) NMR pulse sequence with hypercomplex data acquisition, were carried out with 256 20-μs t_1 increments and 5-s recycle delays. The 2D ^1H-^{31}P heteronuclear correlation (HetCor) NMR experiments were carried out with 100 44-μs t_1 increments and 15-s recycle delays. Lee-Goldburg cross-polarization (LGCP) was used for polarization transfer from ^1H to ^{31}P in both "WISE"[24] and HetCor experiments with contact times of 0.7 and 0.5 ms, respectively. Two-pulse phase-modulation (TPPM) was used for ^1H-^{31}P dipolar decoupling. The hydroxide proton peak at 0.18 ppm and ^{31}P peak at 2.8 ppm in NIST hydroxyapatite were used as secondary chemical shift references to calibrate the ^1H and ^{31}P chemical shifts, respectively. All NMR experiments were carried out at ambient temperature.

H. Scattering

Small-angle x-ray scattering (SAXS) experiments were performed at the 12-ID beam line at the Advanced

Photon Source (APS) in Argonne National Laboratory to elucidate the structure of the polymer-peptide gel nanocomposites. By using 12 keV x-rays ($\lambda = 1.035$ Å), the data were collected at 1-s exposure with a 15 × 15 cm^2 CCD detector at a sample-to-detector distance of 2 m to measure the scattered intensity, and the transmitted intensity was measured using a photodiode buried in the beam stop. The measured 2D data for the gel samples sandwiched between kapton tapes were corrected, azimuthally averaged, and the scattering data was expressed as a function of Q ($4\pi \sin\theta/\lambda$), where 2θ is the scattering angle. To complement the SAXS data that has higher sensitivity for the inorganic phase, small-angle neutron scattering (SANS) was used to highlight the structural features of the copolymer phase in the nanocomposite gels because the neutron-scattering contrast for the polymer phase, when in a deuterated solvent, is much higher than the inorganic phase. To increase the scattering contrast of the copolymer, the gel samples were prepared in D_2O, and the pH was adjusted to 8 by using DCl and NaOD. The samples were sealed in quartz cylindrical cells with a 2-mm path length, and the experiments were performed using the time-of-flight SAND instrument at the Intense Pulsed Neutron Source (IPNS) at the Argonne National Laboratory that yielded data in a Q range of 0.008 to 1 $Å^{-1}$ in a single measurement. The scattering data were corrected following the routine procedures, and the $I(Q)$ was placed on an absolute scale in the units of cm^{-1}.

I. Electron microscopy

TEM, STEM, HRTEM, SAED, and STEM-EDS analyses were performed with a FEI-Tecnai G^2-F20 (FEI Inc., Hillsboro, OR) scanning transmission electron microscope equipped with EDS (EDAX Inc., Mahwah, NJ) using a CCD camera and Digital Micrograph Software (Gatan, Pleasanton, CA). For the STEM analysis, the copolymer and nanocomposite gel samples were diluted with deionized water to obtain 5.0 wt% polymer solutions. Approximately 50 μL of the aqueous sample was placed onto a Formvar-coated copper grid, and the excess solution was wicked away. A negative contrast stain consisting of 1% ammonium molybdate or phosphotungstic acid at pH ~8 was applied. Phosphotungstic acid was used for control samples only (polymer gels without any CaP), whereas ammonium molybdate was used for calcium phosphate nanocomposites. After applying the stain, the excess solution was wicked and the sample was allowed to dry.

IV. RESULTS AND DISCUSSION

A. Polymer characterization

The polymer-peptide attachment was qualitatively characterized using ^{1}H solution NMR. Compared with the spectra of the polymer alone, the additional peaks between 1-2.5 ppm corresponding to the peptide protons compared with the polymer alone ^{1}H NMR spectra confirmed the conjugation of the peptide to the polymer. The conjugation efficiency was determined by subtracting the amount of unreacted peptide measured by RP-HPLC and UV detection from that of the initial amount of peptide used for the conjugation. In the case of Pluronic, the conjugation efficiency was found to be approximately 19.8%, whereas it was found to be approximately 26.6 and 22.9%, for PentaPAA and PentaPZ, respectively.

B. Structure and composition of the inorganic phase

The x-ray diffraction patterns of the as prepared CaP/hydrogel samples and pure HAp (Standard Reference Material® 2910) are shown in Fig. 1. All of the observed peaks can be assigned to HAp with reference to ICCD (JCPDS 9–432) and pure HAp (Standard Reference Material® 2910) as predicted by the calcium phosphate pH-concentration diagram,[25,26] and experimentally shown by

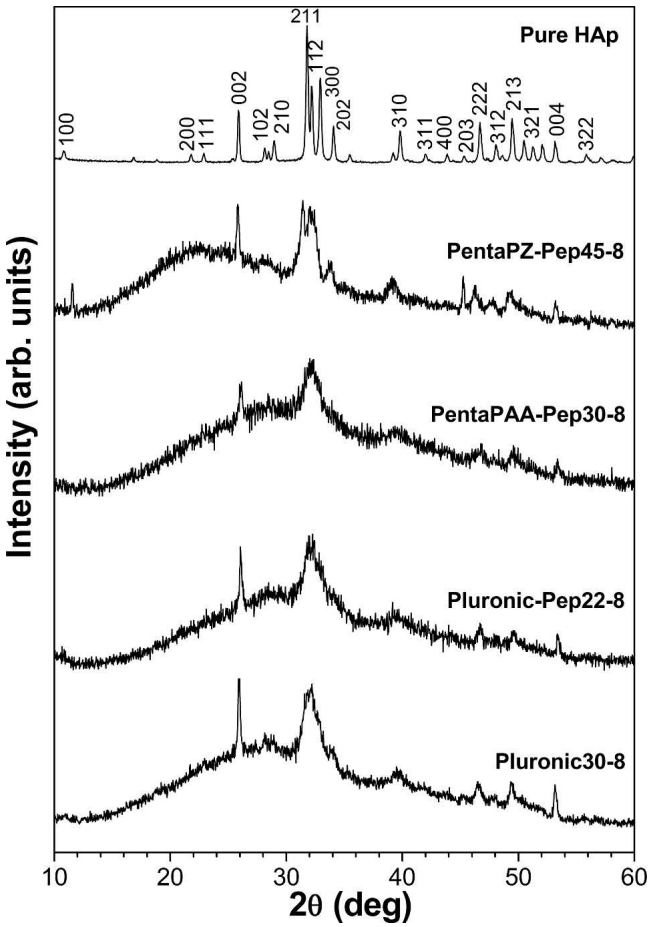

FIG. 1. XRD patterns of as-prepared calcium phosphate/hydrogel nanocomposites PentaPZ-Pep45-8, PentaPAA-Pep30-8, Pluronic-Pep22-8, Pluronic30-8, and pure HAp (Standard Reference Material® 2910).

Yusufoglu and Akinc,[27] with the exception of one very weak peak at $2\theta = 11.7°$ for PentaPZ-Pep45-8. Because brushite is believed to be a precursor in the precipitation of HAp[28,29] and has its most intense peak at $2\theta = 11.7°$ (JCPDS 9-0077), we surmise that this weak peak is likely from brushite.

As seen in Fig. 1, all CaP/hydrogel nanocomposite XRD patterns exhibit similar features and show a broad peak at approximately $2\theta = 32°$ and $2\theta = 26°$, very similar to the XRD patterns of natural human bone and dentine.[30,31] The broad peak at approximately $2\theta = 32°$ is a composite band resulting from three of the most intense peaks of HAp [(211), (112), and (300) planes]. Moreover, the broad peaks are indicative of nanocrystalline or/and the poorly crystalline nature of the HAp, and the broad background is possibly due to the amorphous nature of the polymer matrix. Furthermore, HAp/hydrogel samples were vacuum dried, and the polymer was removed by dissolving in deionized water at ~1 °C. The XRD diffraction patterns of the vacuum-dried gel nanocomposite and polymer-free samples are illustrated in Figs. 2 and 3, respectively. HAp precipitated in the absence of polymer is also included in Fig. 3. XRD patterns of vacuum-dried samples showed that some HAp reflections were absent. This is believed to be due to the preferential orientation of HAp crystallites in the polymer matrix during vacuum drying or sample preparation for XRD analysis. Furthermore, vacuum-dried polymer solutions prepared in deionized water (control solutions) were also analyzed by XRD (data not shown). The diffraction peaks observed in Fig. 2 at 2θ ~19.5 and 2θ ~23.5 were ascribed to polymer peaks that appeared after vacuum drying. The XRD patterns of samples with polymer removed after vacuum drying (designated as "washed" samples) are shown in Fig. 3. The XRD patterns of the washed samples are similar to those of as-prepared CaP/hydrogel samples, with the exception that they are of higher intensity and also contain additional

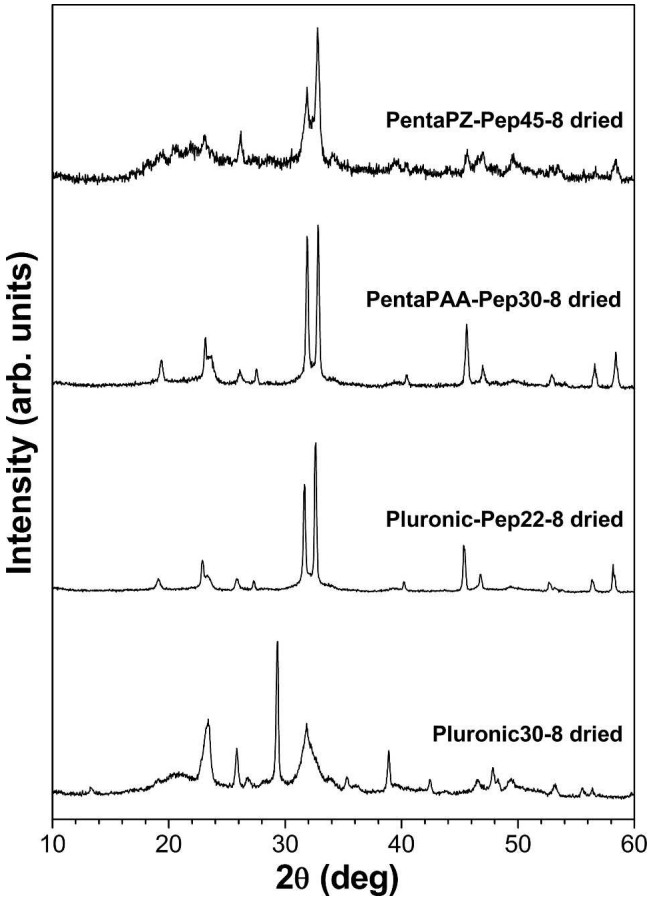

FIG. 2. XRD patterns of vacuum-dried PentaPZ-Pep45-8, PentaPAA-Pep30-8, Pluronic-Pep22-8, and Pluronic30-8.

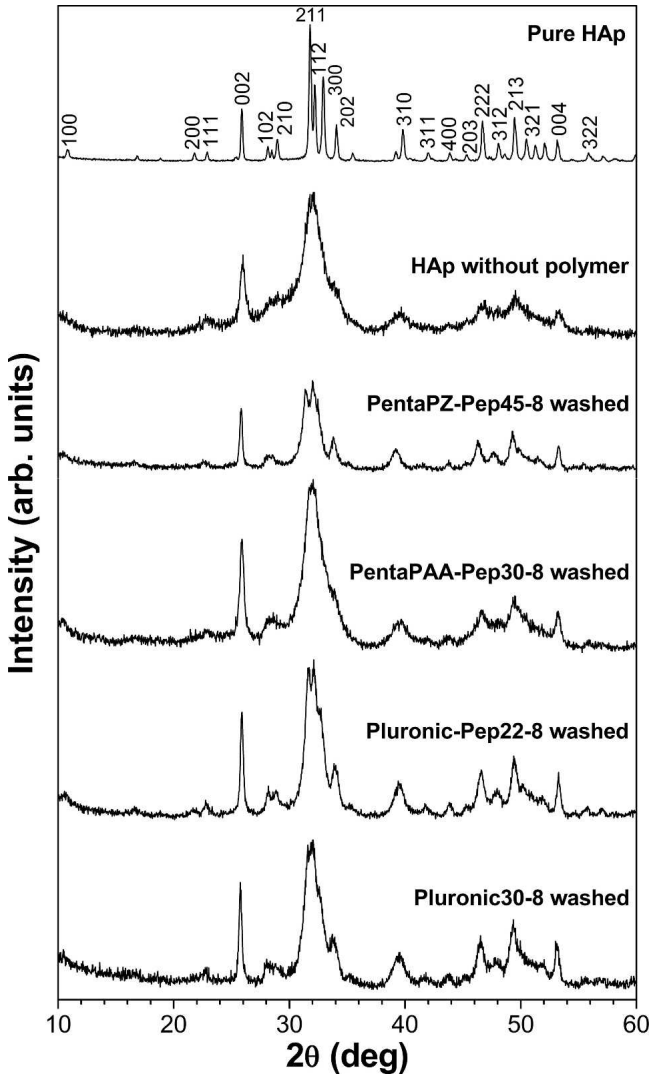

FIG. 3. XRD patterns of washed PentaPZ-Pep45-8, PentaPAA-Pep30-8, Pluronic-Pep22-8, Pluronic30-8, HAp precipitated from an aqueous solution at pH ~8 without any polymer and Pure HAp (Standard Reference Material® 2910).

peaks that can all be assigned to HAp. In addition, comparison of the XRD results in Figs. 2 and 3, supports the conclusion that vacuum drying may cause preferential orientation of HAp crystals in the polymer matrix.

To further characterize the HAp/hydrogel nanocomposite samples, FTIR surface analysis was performed, as illustrated in Figs. 4 and 5.

The differences between hydrogel prepared in calcium phosphate solutions and in deionized water as well as pure HAp (Standard Reference Material® 2910) spectrum can be seen in Fig. 4. The FTIR spectra in the present study were carefully compared with those reported earlier[32–34] and pure HAp (Figs. 4 and 5). Pure HAp shows phosphate peaks at 965 cm^{-1}, 470 cm^{-1}, between 1050-1095 cm^{-1} and 565-602-635 cm^{-1} (three sites) for ν_1, ν_2, ν_3, and ν_4, respectively. For our vacuum-dried nanocomposite samples, these peaks appear at approximately 961 cm^{-1}, 454 cm^{-1}, 1038 cm^{-1}, and 566-601 cm^{-1} (two sites). Infrared spectroscopy analysis showed major phosphate peaks, confirming the formation of HAp in the nanocomposites. Furthermore, the bands at approximately 1410 and 1460 cm^{-1} might be ascribed to CO_3.[35,36] However, in the presence of polymer, CO_3 peaks cannot be assigned with certainty because of the strong C-H and COO^- bands (from the polymer) in the same spectral regions. Possible assignments of all adsorption bands in Figs. 4 and 5 are listed in Table I. Because some of the CO_3 and PO_4 absorption bands overlap with the polymer-related peaks (C-H and C-O bands), FTIR analysis was also performed for the

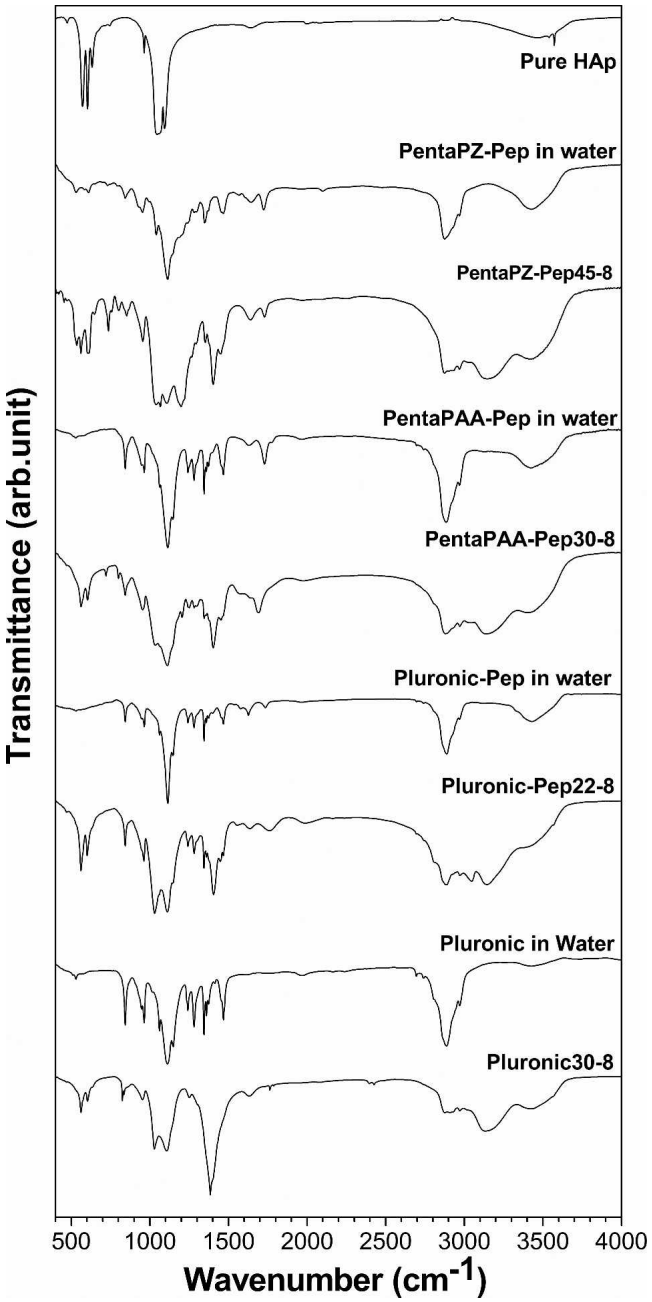

FIG. 4. FTIR spectra of the vacuum-dried HAp/nanocomposite samples, corresponding vacuum-dried polymer/water samples (control solutions), and pure HAp (Standard Reference Material® 2910).

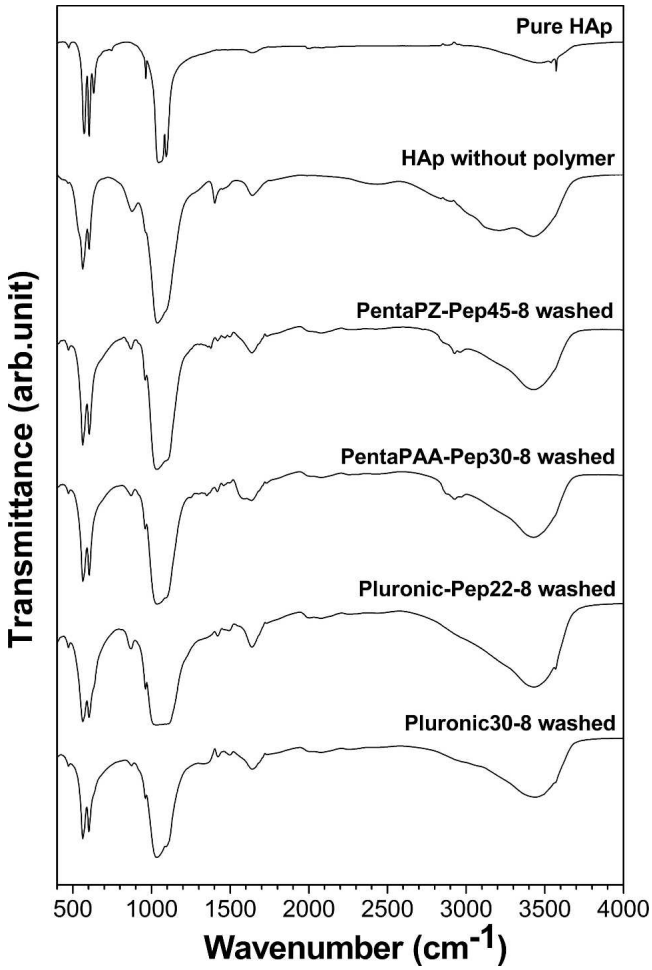

FIG. 5. FTIR spectra of the polymer-removed HAp/nanocomposite samples, HAp precipitated without any polymer, and Pure HAp (Standard Reference Material® 2910).

nanocomposite samples with the polymer removed (designated as "washed samples"). The spectra of the washed samples as well as HAp precipitated from an aqueous solution without any polymer were shown in Fig. 5. The observed absorption peaks correspond to HAp.[25,27,37,38]

When the HAp was precipitated without any polymer under the same experimental conditions, small bands assigned to CO_3 were detected approximately 873, 1410, and 1465 cm^{-1}, as seen in Fig. 5. The positions of these peaks indicate that the CO_3 groups may have incorporated into the HAp crystal structure and replaced PO_4.[27,33,35,39,40] Carbonate substitution most probably arises from the ion exchange with dissolved CO_2 from the atmosphere during the dissolution, stirring, and reaction processes. However, further work is required to elucidate the source of CO_2 and the exact mechanism of substitution, which are not the focus of the present study. Even though the samples were dried under vacuum, a broad water peak was observed at approximately 3400 cm^{-1} that suggests that HAp binds water. This broad H_2O band from 3600 to 3100 cm^{-1} dominates both spectra in Figs. 4 and 5, masking the OH peak of HAp in this region.

Moreover, as seen from Fig. 5, after extracting the polymer by washing the vacuum-dried samples, all of the PO_4-related peaks can be observed more clearly. The phosphate bands were generally broader, probably because of the small crystallite sizes. From the general view of FTIR analysis, it can be concluded that the mineral phase is HAp in the synthesized CaP/nanocomposite samples, which is consistent with XRD and NMR results.

As-prepared CaP/hydrogel nanocomposite samples were subjected to thermogravimetric analysis to determine the actual content of the mineral phase, which is confirmed to be HAp from various characterization methods in the present study (Fig. 6). Mainly three ranges of mass loss can be assigned to thermogravimetric analysis of the gel samples.[30,44,45] Removal of physically and chemically adsorbed water and possibly lattice water takes place from room temperature to approximately 200 °C. Weight loss related to the pyrolysis of the polymer is observed between 200 and 400 °C. At approximately 400 °C, only the inorganic phase (HAp) remains. If HAp has some incorporated carbonate in the form of carbonated apatite, there will be a weight loss above 400 °C due to the CO_3 removal from the HAp structure.[25,27,44,45] A slight mass loss between the temperature range of 400–600 °C (Fig. 6) possibly corresponds to the decarboxylation of the HAp, releasing $CO_{2(g)}$, which is consistent with the findings from FTIR analysis. Pure HAp is stable up to 1200 °C, and decomposition of HAp is not expected under our experimental conditions.[25,41] Therefore, TGA makes it possible to determine the mineral content in the nanocomposites. The analysis of Fig. 6 showed significant inorganic fractions, approximately 45 wt% for Pluronic-Pep22-8, 40 wt% for PentaPAA-Pep30-8, 35 wt% for Pluronic30-8, and 30 wt% for PentaPZ-Pep45-8. The inorganic contents estimated from TGA results are based on the mass of the dried hydrogel at ~200 °C as 100%, and the results are in good agreement with the theoretically calculated values. In general, the inorganic content in the present study is significantly larger than the 6-5 wt% observed in our previous studies of calcium phosphate formation on cationic and polar templates[16] without hydroxyapatite-binding peptides.

TABLE I. The possible assignments of FTIR peaks present in Figs. 4 and 5.[25,41–43]

Group frequency (cm^{-1})	Assignment
3570-3200 (broad)	Hydroxy group, H-bonded OH stretch
3430 (broad)/1620	Water absorption bands
2970/2885	Methyl C-H asym./sym. stretch
1650-1550	N-H bend
1610-1550/1420-1430 and 960-850	Carboxylate (carboxylic acid salt) and H bonded O-H out-of-plane bending
1465-1430/1380-1330	Methyl C-H asym./sym. bend
1300–700	Methyne C-H vibrations
1250 + 890-800	Epoxy (C-O-)
1210-1150	C-N stretch
1150-1050	Alkyl-substituted ether, C-O stretch (C-O-C)
1050	C-O primary alcohol, C-O stretch
871/1420/1475	Carbonate ν_2 / ν_{3a} / ν_{3b} (for B-CO_3HAp)
710-685	Thiol or thioether, CH_2-S- (C-S stretch)
470/565-602-635/965/1050-1095	Phosphate bands of HAp ν_2 / ν_4 / ν_1 / ν_3

C. NMR identification of phosphates

Figure 7 shows direct polarization (DP) and cross-polarization (CP) ^{31}P NMR spectra of Pluronic30-8,

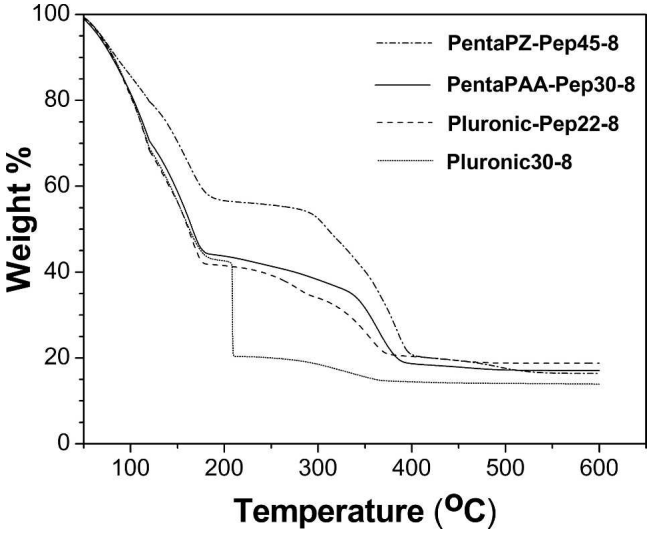

FIG. 6. TGA traces of PentaPZ-Pep45-8, PentaPAA-Pep30-8, Pluronic-Pep22-8, and Pluronic30-8 hydrogel samples.

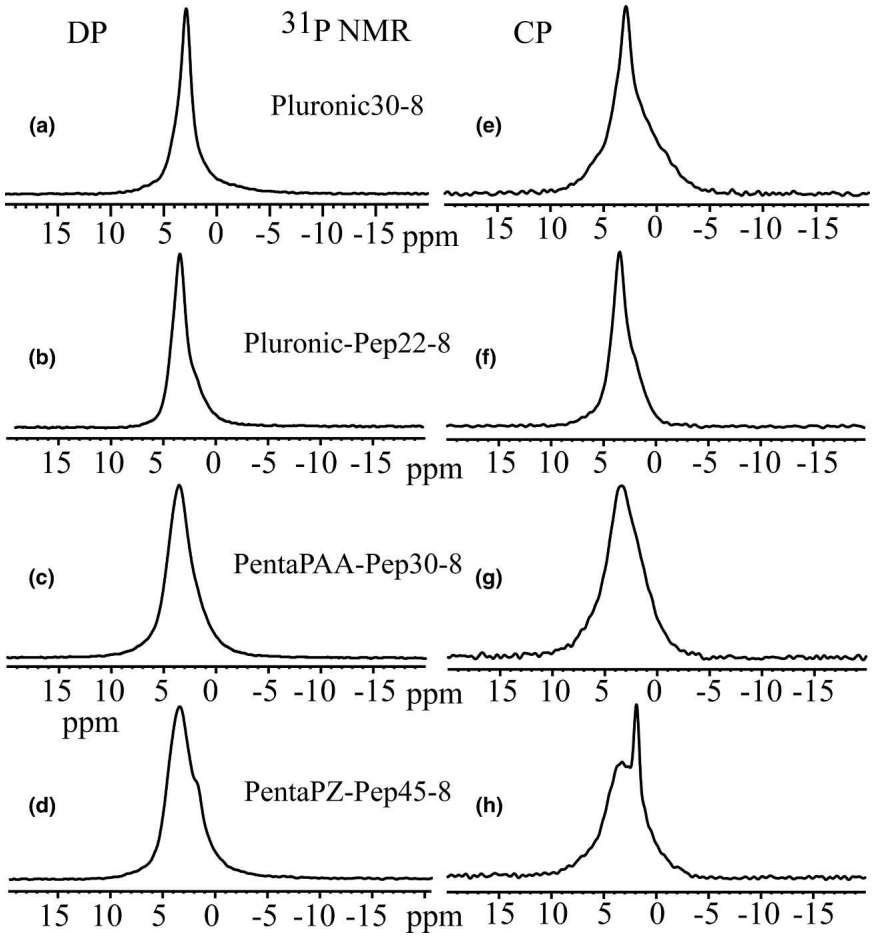

FIG. 7. (left column) DP/MAS and (right column) CP/MAS ^{31}P NMR spectra of synthesized nanocomposites. (a) and (e) Pluronic30-8. (b) and (f) Pluronic-Pep22-8. (c) and (g) PentaPAA-Pep30-8. (d) and (h) PentaPZ-Pep45-8.

Pluronic-Pep22-8, PentaPAA-Pep30-8, and PentaPZ-Pep45-8. For all samples except PentaPZ-Pep45-8, the spectra show only one resolved band. Its position agrees with the 3-ppm chemical shift of hydroxyapatite,[46] although the linewidth is larger than for ideal hydroxyapatite. For PentaPZ-Pep45-8, the CP spectrum shows two peaks, see Fig. 7(h). Whereas the broad component is again hydroxyapatite, the sharp peak can be tentatively assigned to brushite, based on its chemical shift.[46] The quantitative DP ^{31}P NMR spectrum of PentaPZ-Pep45-8 indicates that brushite is only a minor component, compared with hydroxyapatite. For all samples, the DP and CP spectra showed similar features, but the lines in the CP spectra are broader. The likely reason is an enhanced contribution of signals from HPO_4^{2-} ions and PO_4^{3-} hydrogen bonded to H_2O in the CP spectrum.

These tentative assignments of the ^{31}P resonances are confirmed by the proton peak positions in 2D ^{1}H-^{31}P correlation spectra without spin diffusion [Figs. 8(a), 9(a), and 10(a)]. The OH^- proton of hydroxyapatite is detected around 0.2 ppm, whereas the broad signal near 7 ppm is consistent with H_2O hydrogen bonded to PO_4^{3-}, and the even broader band around 12 ppm must be assigned to HPO_4^{2-}. For PentaPZ-Pep45-8, the 6.5- and 10-ppm ^{1}H signals of the sharp 1.4-ppm ^{31}P peak agree with those of H_2O and HPO_4^{2-}, respectively, in brushite from the literature.[47]

D. NMR evidence of nanocomposite formation

The formation of nanocomposites can be proved by 2D ^{1}H-^{31}P heteronuclear correlation NMR experiments with ^{1}H spin diffusion, where the presence of cross-peaks between polymer protons and inorganic phosphate within a few tens of milliseconds proves the intimate contact between organic and inorganic phases that is characteristic of nanocomposites.[16,48] Figure 8(a) shows a series of 2D HetCor ^{1}H-^{31}P spectra of PentaPAA-Pep30-8 with spin diffusion mixing times of 0.05, 50, and 500 ms. Cross-sections along the ^{1}H dimension, taken at 2.8 ppm in the ^{31}P dimension, are shown in Fig. 8(b). First, only OH^- signals in the inorganic phase and a broad band of H-bonded H_2O appear. Within 50 ms, the polymer proton

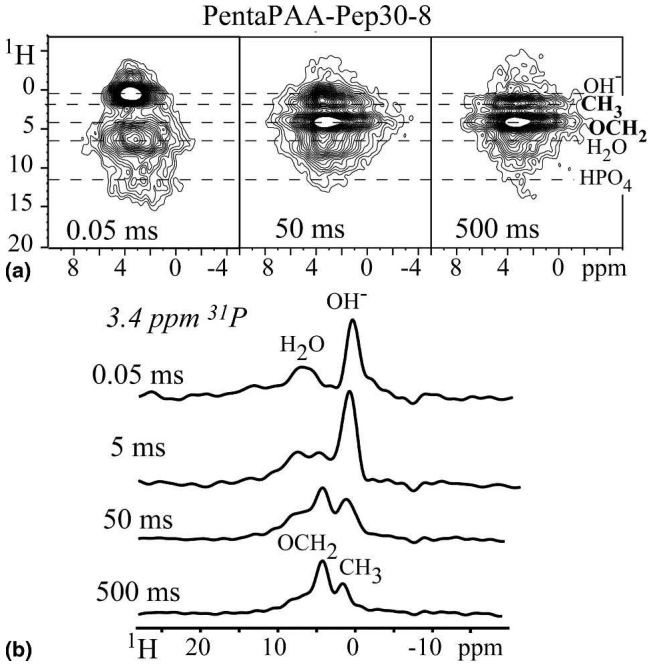

FIG. 8. (a) 2D ^{1}H-^{31}P HETCOR NMR spectra of PentaPAA-Pep30-8 with spin diffusion mixing times of 0.05, 50, and 500 ms. (b) Cross-sections from the 2D spectra at 2.8 ppm (^{31}P).

peaks (CH_3 and OCH_2) show up, and they become completely dominant after 500 ms of spin diffusion; this proves the formation of a nanocomposite. Given the small proton concentration in hydroxyapatite, spin diffusion is relatively slow. The inorganic particles must be less than 10-nm thick, based on comparisons with spin diffusion in bone, where the inorganic crystals are ~3-nm thick.

A series of 2D HetCor ^{1}H-^{31}P spectra of PentaPZ-Pep45-8 and cross-sections at HAp and brushite resonances are shown in Fig. 9. Again, equilibration is observed within 500 ms for the HAp component, whereas the brushite cross-sections change little. This shows that the HAp is part of a nanocomposite, whereas brushite forms larger crystals. The heteronuclear correlation experiment can also be performed with homonuclear ^{1}H decoupling in the ω_1 dimension, using a pulse sequence closely resembling that of WISE NMR.[24] This version of the experiment is simpler, requires less radio-frequency irradiation, provides unscaled ^{1}H chemical shifts, and may yield higher resolution for mobile segments such as those of the Pluronic blocks. A series of "WISE" ^{1}H-^{31}P spectra of Pluronic-Pep22-8 are shown in Fig. 10. The OH^- and polymer OCH_2 and CH_3 peaks are well

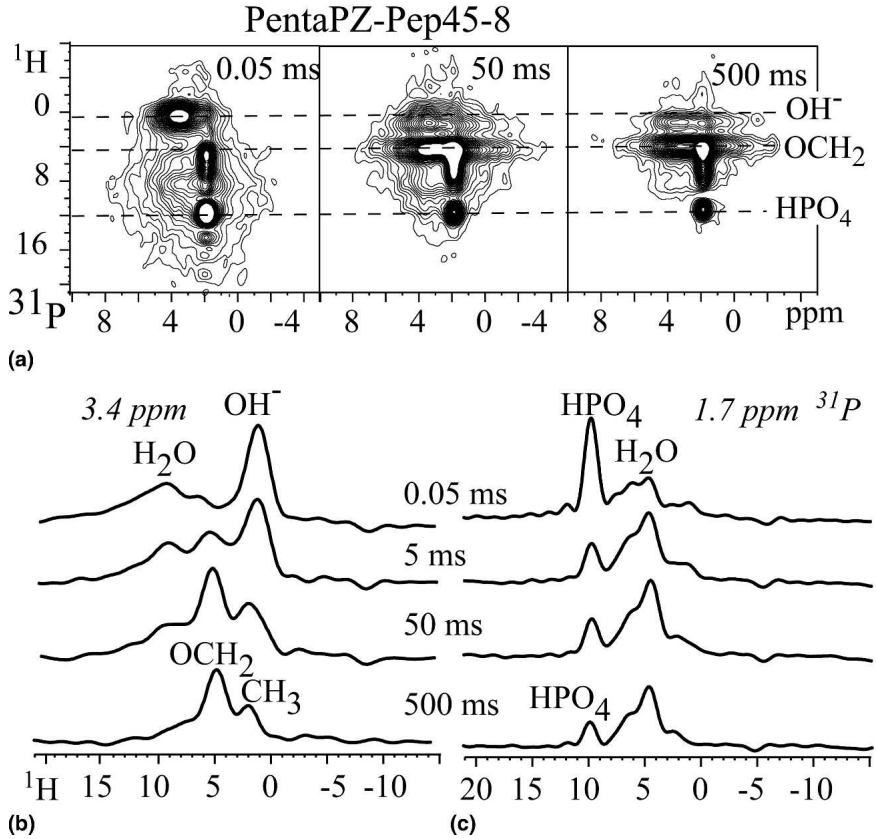

FIG. 9. (a) 2D ^{1}H-^{31}P HETCOR NMR spectra of PentaPZ-Pep45-8 with spin diffusion mixing times of 0.05, 5, 50, and 500 ms. (b) and (c) Cross-sections from the 2D spectra at 1.4 and 2.8 ppm (^{31}P).

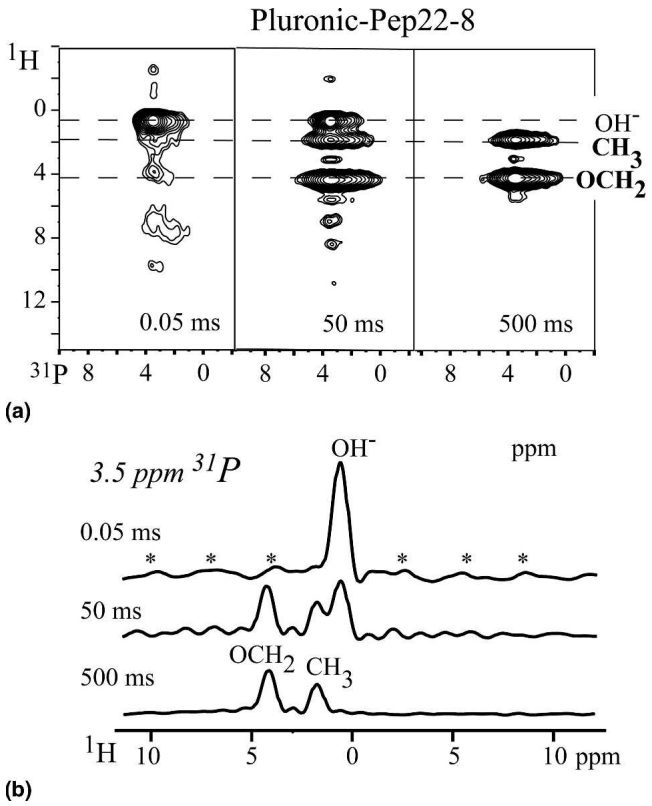

FIG. 10. (a) 2D ^{1}H-^{31}P "WISE" NMR spectra of Pluronic-Pep22-8 with spin diffusion mixing times of 0.05, 50, and 500 ms. (b) Cross-sections from the 2D at 2.8 ppm (^{31}P). The strongly coupled component shows sidebands, marked by asterisks.

resolved, and the formation of a nanocomposite is easily proven. Similar series of spectra were obtained for Pluronic30-8, PentaPAA-Pep30-8, and the HAp component in PentaPZ-Pep45-8, confirming nanocomposite formation in these materials.

E. Nanostructures of organic and inorganic phases from SAXS/SANS

By virtue of drastically different interaction of neutrons and x-rays with matter, SANS and SAXS serve as excellent complementary tools to investigate the nanostructural features in multicomponent hybrid polymer/inorganic nanocomposites. The complementarity can be clearly seen in Fig. 11, wherein the SANS and SAXS profiles of the neat and corresponding nanocomposite gels are quite different. Whereas the SANS data of both the polymer and the nanocomposite gel samples look similar and exhibit peaks, the SAXS data show peaks only for the neat polymer, but power-law scattering for the nanocomposites due to the major contribution of the inorganic phase in the latter. The reason for this is that the SAXS signals of nanocomposites are over 3 orders of magnitude higher than the neat polymers. In the SAXS data, we observe signatures for the average size of the inorganic nanocrystals in the high Q region and power-law scattering in the low Q region, representing their connectivity and correlations in the polymer matrix. In general, the power-law exponent in the low Q region suggests the connectivity between the fundamental particles, the size of which can be derived from the scattering intensity in the high Q region. The absolute value of the power-law exponent in the low Q region will assume values in the vicinity of 1, 2, and 3 for the 1D (rod), 2D (sheet), and 3D morphologies at $QR_g \gg 1$, where R_g is the radius of gyration of the whole particle. In the case of mass fractal objects, the absolute value of the power-law exponent becomes a noninteger in the range of 1 to 3, the larger the exponent value the denser the distribution of the fundamental particles in the matrix. Although real-space images would aid the proper interpretation of the small-angle scattering data, modified Guinier analyses for the cross-sectional dimensions help to resolve between a mass fractal object versus a rod when the power-law exponent has a value in the vicinity of 1 and a sheet when it has a value around 2. We will use these ideas in the interpretation of the SAXS data below.

For the neat Pluronic gel, both the SANS [Fig. 11(a)] and the SAXS [Fig. 11(b)] data show diffraction peaks at Q/Q* values of 1, $\sqrt{3}$, 2, and $\sqrt{8}$ corresponding to the FCC packing of spherical micelles. The presence of peaks in the SANS data at similar repeat distances for the gels of the neat copolymers and the corresponding nanocomposites indicate that the growth of the inorganic phase has little effect on the long-range order and morphologies of the polymer phase. This is consistent with the fact that crystals that nucleate in the interstitial regions will grow around the polymer phase and get connected. The SANS data of the Pluronic30-8 and Pluronic-Pep22-8 nanocomposites clearly show power-law scattering in the low Q regions due to the presence of inorganic structures in addition to the peaks associated with the polymer morphology. For the PentaPAA system, the SANS data for both the neat polymer and the nanocomposite gels [Fig. 11(c)] show BCC ordering with d-spacing around 16 nm, and the nanocomposite exhibits power-law scattering in a small low Q region. The SANS data for the PentaPZ-Pep samples indicate a HCPC structure corresponding to the diffraction peaks at Q/Q* values of 1, $\sqrt{3}$, $\sqrt{7}$, and $\sqrt{12}$ for the neat polymer as well as the nanocomposite samples, with the d-spacing of 20 nm. In this case, the upturn in the low Q region was less pronounced when compared with the other composites.

Based on its high sensitivity to the inorganic phase, we use SAXS data to evaluate nanostructural features in the nanocomposites. The I(Q) curves of these nanocomposite samples are similar to those of bone.[49] In the case of Pluronic30-8 [Fig. 11(b)], the characteristic length scale of the inorganic phase is ~4.86 nm and a $Q^{-2.183}$ power-law scattering in the low Q region. On the other hand, for

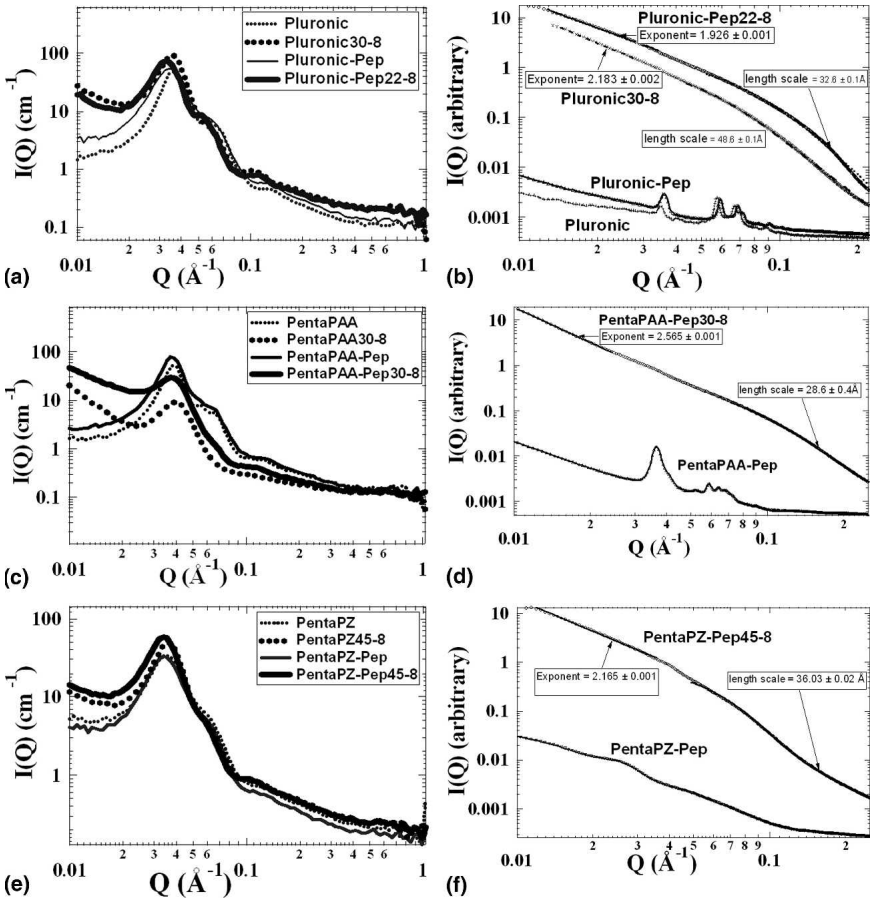

FIG. 11. (a) SANS and (b) SAXS of gels of neat Pluronic, Pluronic-Pep, and corresponding nanocomposites at pH 8.0; (c) SANS and (d) SAXS of gels of neat PentaPAA-Pep and corresponding nanocomposite; (e) SANS and (f) SAXS of the gels of PentaPZ-Pep and corresponding inorganic nanocomposite. The high Q regions of the SAXS data were fitted using a combined equation consisting of an exponential and a power law, and the low Q data were fitted using a power law.

the Pluronic-Pep22-8 gel, the characteristic length scale of the inorganic phase is ~3.26 nm, which is significantly smaller, and a $Q^{-1.926}$ power-law scattering in the low Q region. The power-law exponent in the vicinity of 2 implies that the whole particle has a sheet-like morphology, which is consistent with the TEM of the nanocomposites presented later. Although we cannot determine the largest dimension of the sheet-like objects with the limited Q range of the small-angle scattering data, we can use the modified Guinier analysis for a sheet-like morphology by plotting $\ln(Q^2.I)$ versus Q^2 and fitting a straight line in a Q region where $Q_{max}.T < 0.28$, where T is the average thickness of the sheet-like particles. The thickness of the sheet-like objects in Pluronic30-8 and Pluronic-Pep22-8 gels falls in the range of 4 to 5 nm. For a given block copolymer, we also observe that the nanocomposite with the peptides exhibits higher scattering intensity than that without the peptide, suggesting that the peptide may have some influence in significantly enhancing the growth and nucleation of the inorganic phase during the nanocomposite formation. These results are consistent with the higher inorganic content measured for the peptide containing nanocomposites. Figure 11(d) shows the SAXS data for the neat PentaPAA-peptide and the corresponding nanocomposite. Consistent with the SANS data, the neat polymer shows several peaks for a highly ordered BCC phase with diffraction peaks at Q/Q* values of 1, $\sqrt{2}$, $\sqrt{3}$, and 2, whereas the nanocomposite exhibits the presence of nanocrystals with an average characteristic length scale of ~3 nm and a $Q^{-2.565}$ power-law scattering. In contrast to the Pluronic and PentaPAA systems, the neat PentaPZ gel [Fig. 11(f)] shows only weak peaks in the SAXS data. This discrepancy could be due to the potential for the samples on kapton tape to dry during the SAXS measurement, whereas the samples for the SANS measurement were contained in sealed quartz cells. The PentaPZ-Pep45-8 nanocomposite shows the presence of nanocrystals with an average length scale ~3.6 nm and a $Q^{-2.165}$ power-law scattering in the low Q region. Modified Guinier analysis of these nanocomposites revealed a thickness in the range of 4 nm.

In summary, SANS and SAXS data clearly show that both the polymer and the nanocomposite structures have long-range order with nanometer-size morphology. This

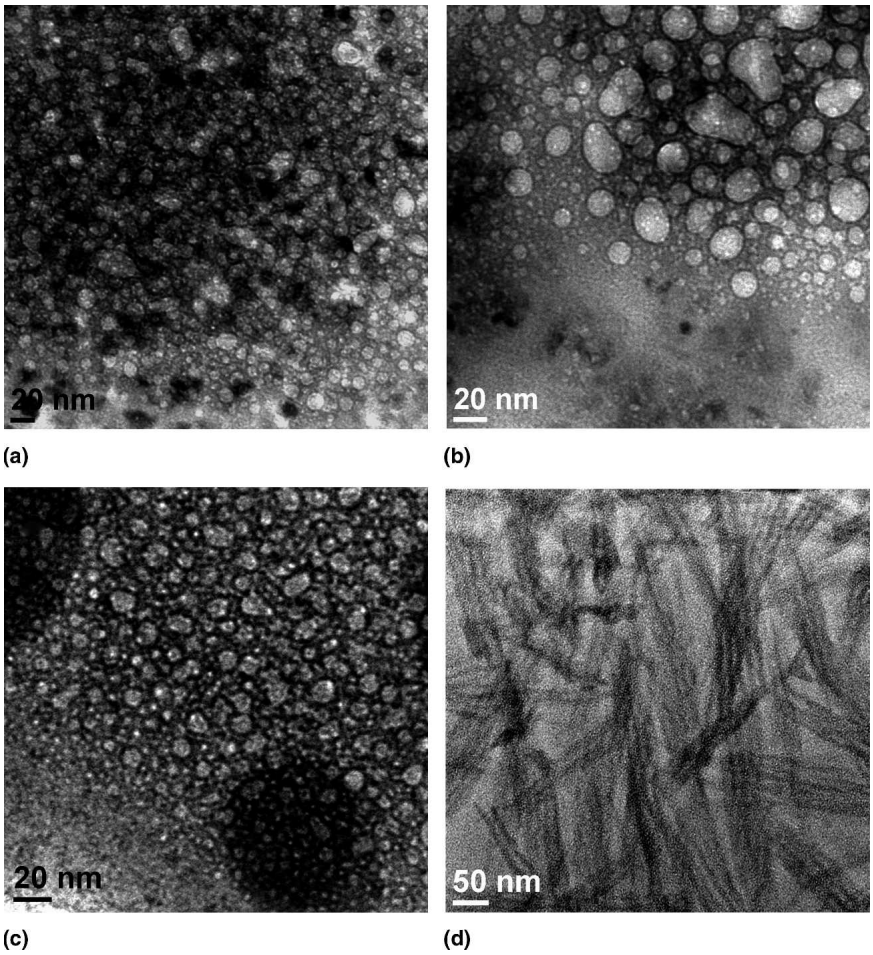

FIG. 12. STEM/HAADF micrographs of 5 wt% of polymer solutions prepared in deionized water and stained; (a) Pluronic, (b) Pluronic-Pep, (c) PentaPAA-Pep, and (d) PentaPZ-Pep. Light regions: Polymer.

is in good agreement with the NMR data, where it was found that the polymer and inorganic are in close contact and in the nanometer-size range. Furthermore, the conjugated peptide with the polymer does significantly enhance the growth and nucleation of the inorganic compared with the polymer templates without the peptide.

Scanning transmission electron micrographs (STEM) of 5 wt% Pluronic, Pluronic-Pep, PentaPAA-Pep, and PentaPZ-Pep prepared in deionized water are illustrated in Fig. 12. As seen from the STEM data in Fig. 12, PentaPZ-Pep polymer solution revealed rod-like structures, whereas all other polymers showed spherical micelles, in agreement with the SAXS and SANS results. The electron beam damage of the polymer precludes the size determination of the spherical micelles by STEM. However, earlier SAXS and SANS revealed that the micelles were approximately 15 nm in diameter, which is also consistent with our previous studies.[16]

Extensive TEM studies were performed on the HAp nanocomposite samples, and all micrographs are illustrated in Figs. 13 and 14. Figure 13 shows bright-field (BF) TEM images and corresponding SAED patterns of the HAp/hydrogel nanocomposite samples diluted to 5 wt% polymers with deionized water. In addition, HAp synthesized from an aqueous solution without any polymer added and a HAADF image of Pluronic-Pep22-8 is also shown in Fig. 13. Figure 13(a) reveals that HAp in Pluronic30-8 nanocomposite is constituted of thin, elongated, plate-like crystals with a mean length and width of approximately 110 and 20 nm, respectively. HAp nanocrystals of PentaPAA-Pep30-8 are also of plate-like shape but with shorter mean length and irregular edges [Fig. 13(b)]. This morphology is very similar to the apatite crystals from the mid-diaphyses of a 19-week-old human fetal femur.[50] Furthermore, the morphology of the Pluronic-Pep22-8 nanocomposite is quite similar to that observed for the Pluronic30-8. Although the nanocrystals appears to be more needle-like for Pluronic-Pep22-8 in Fig. 13(c), the apparent elongated crystals are actually plate-like but curled and viewed edge-on as seen from the HAADF image shown in Fig. 13(d). It seems that curled plate-like nanocrystals appear to be needle-like when tilted and viewed on edge [Fig. 13(d)]. The variable morphology of the nanocrystals is difficult to

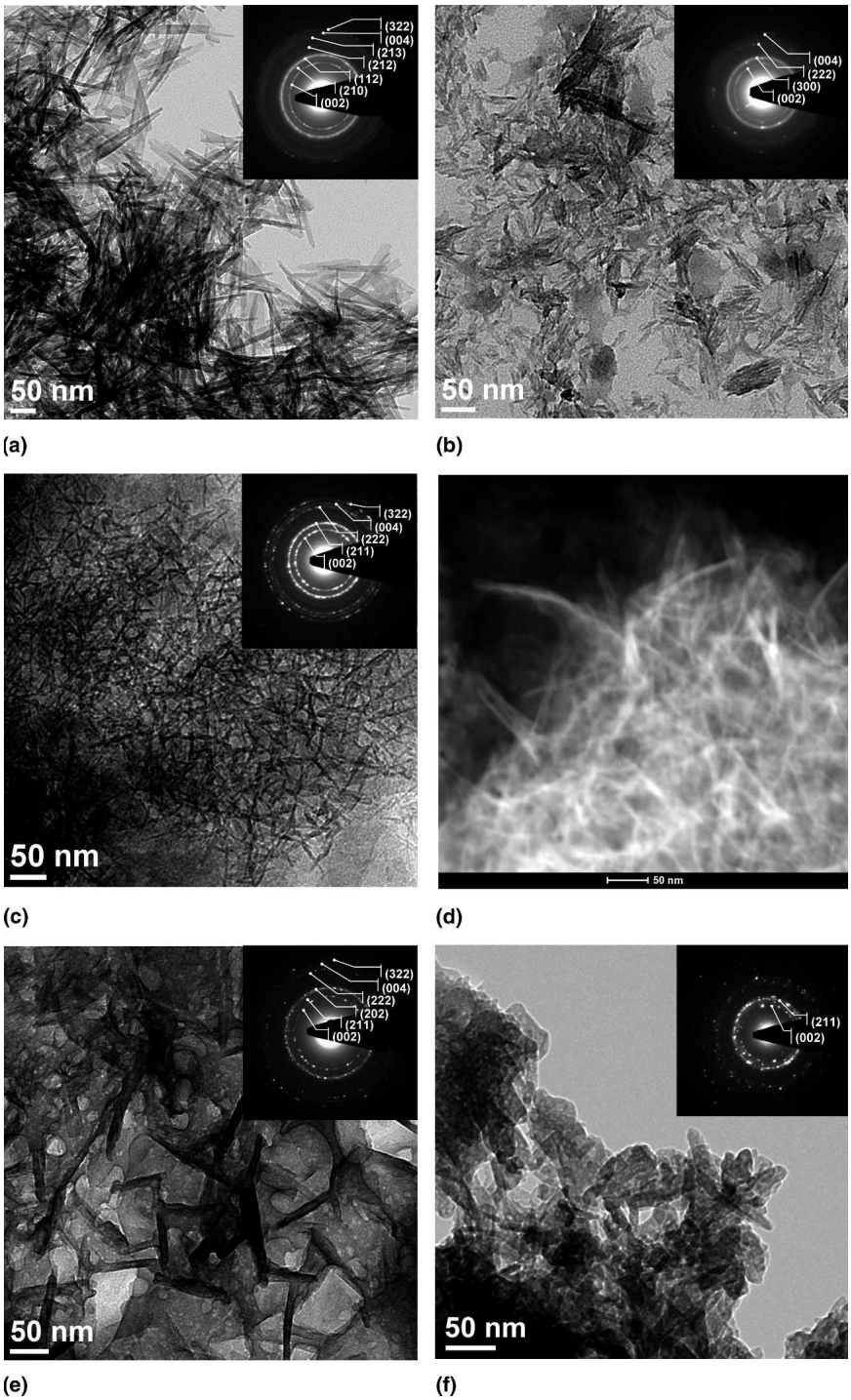

FIG. 13. BF-TEM images and corresponding SAED patterns of 5 wt% (a) Pluronic30-8, (b) PentaPAA-Pep30-8, (c) Pluronic-Pep22-8, (e) PentaPZ-Pep45-8, and (f) HAp nanocrystals obtained by direct synthesis from an aqueous solution at pH ~8 without any polymer. (d) STEM image of Pluronic-Pep22-8.

describe, and they vary from ~30 to 80 nm in length and ~10 to 25 nm in width. Figure 13(e) reveals the morphology of HAp nanocrystals in PentaPZ-Pep45-8, which is also similar to other HAp nanocomposite samples. In general, the morphology of HAp nanocomposites observed in the present study is quite similar to those of various other HAp nanocomposites seen in the literature.[33,34] However, the morphology of the HAp crystals synthesized without any polymer [Fig. 13(f)] looks significantly different than that observed for HAp/hydrogel nanocomposite samples. Figure 13(f) shows that HAp nanocrystals in polymer-free sample resulted in bulk

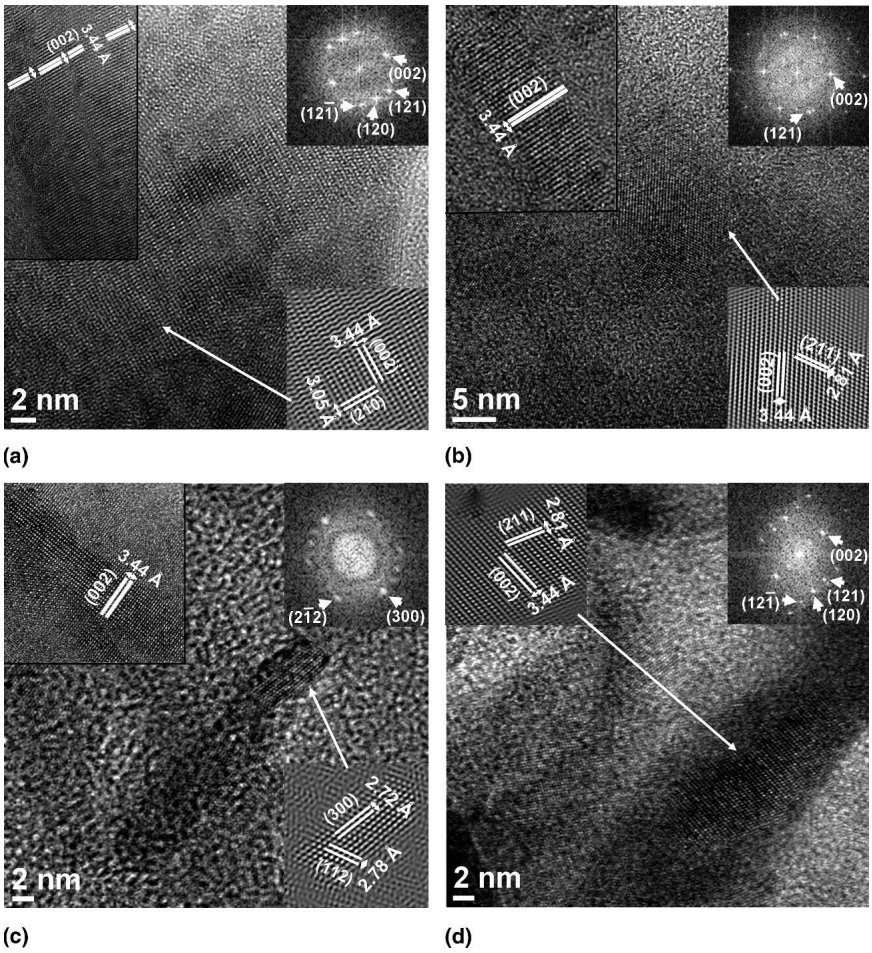

FIG. 14. HRTEM images of (a) Pluronic30-8, (b) PentaPAA-Pep30-8, (c) Pluronic-Pep22-8, and (d) PentaPZ-Pep45-8. The upper right and lower insets show the FFT patterns and filtered inverse-FFT images, respectively, while the upper left insets show HRTEM images taken from plate-like crystals in longitudinal sections.

precipitation of plate-like crystals. It seems that in the presence of the polymers, the morphology of HAp nanocrystals is more elongated and plate-like than that without any polymer.

The upper insets in Fig. 13 demonstrate SAED patterns of HAp/hydrogel nanocomposites and HAp synthesized without any polymer (polymer-free sample). SAED patterns with prominent diffraction rings clearly reveal a well formed polycrystalline phase. Furthermore, the diffraction rings are all associated with HAp (JCPDS 9–432), and corresponding planes of HAp can be seen in the insets of Fig. 13. The findings from the SAED patterns are consistent with those obtained from the XRD study. Although the SAED pattern of the polymer-free sample [Fig. 13(f)] shows clearly distinct spots, they did not form well defined rings, with the exception of the (211) plane of HAp, as shown in Fig. 13(f). However, the SAED patterns of HAp nanocomposites showed strong small spots forming well defined rings, which indicates the preferential alignment of nanocrystals.

In Fig. 14, HRTEM micrographs showing nanocrystals surrounded by amorphous phase (polymer) also confirm the existence of the HAp phase in the nanocomposites. The upper right and lower insets in Fig. 14 illustrate the FFT pattern and filtered inverse-FFT image, respectively. The FFT pattern of the nanocrystals shown in the upper right inset was closely related to the FFT pattern of hydroxyapatite phase observed along the [2$\bar{1}$0] zone axis for Pluronic30-8, PentaPAA-Pep30-8, PentaPZ-Pep45-8, and along the [021] zone axis for Pluronic-Pep22-8. Moreover, the upper left insets of Fig. 14 show HRTEM images taken from different regions. All HRTEM images in Fig. 14 demonstrate that the crystal lattice planes are well aligned, albeit with some defects. The crystal planes of HAp determined in these images were indexed by comparing the measured d spacings and interplanar angles with the calculated values of HAp (JCPDS 9–432). The results from HRTEM agree well with those obtained from XRD and SAED study. The diffraction peaks of all crystal planes determined from HRTEM analysis are also present in the XRD and

TABLE II. Summary of characterization studies of the biomimetic hydrogel/CaP nanocomposites.

	XRD	XRD, FTIR	NMR	STEM, HRTEM, SAED	SAXS, SANS	TGA
Samples	Gel	Vacuum dried	Vacuum dried	Gel diluted to 5 wt% Polymer	Gel morphology	Dried
Pluronic30-8	HAp	HAp	HAp	Elongated plate-like HAp	FCC	35 wt% CaP
Pluronic-Pep22-8	HAp	HAp	HAp	Elongated plate-like HAp	FCC	45 wt% CaP
PentaPAA-Pep30-8	HAp	HAp	HAp	Elongated plate-like HAp	BCC	40 wt% CaP
PentaPZ-Pep45-8	HAp/Brushite	HAp	HAp/Brushite	Elongated plate-like HAp	HCPC	30 wt% CaP

SAED patterns of the nanocomposites. Furthermore, the upper left insets in Fig. 14 show clearly columnar growth morphology and HRTEM images of plate-like crystals in longitudinal sections reveal a lattice spacing of ~3.4 Å, corresponding to the interplanar spacing of (002) planes for hexagonal HAp (Fig. 14). This is evidence of the fact that the growth of the elongated plate-like nanocrystals occurs along the c-axis direction of HAp. As can be seen from the XRD diffraction patterns in Fig. 1, the relatively high intensity of the (002) and (004) reflections also supports the notion that the growth of the elongated plate-like nanocrystals occurs along the c-axis direction of HAp. In addition, prominent diffraction rings corresponding to (002) and (004) planes of HAp were also observed in all SAED patterns of the nanocomposites, which might also indicate a c-axis growth direction of HAp. This kind of orientation is very similar to that in vertebrate bone.[51] Moreover, the atomic calcium to phosphorous ratio of HAp in nanocomposites was determined by STEM-EDS measurements to be approximately 1.73 ± 0.09, which is close to the stoichiometric value of pure HAp [$Ca_{10}(PO_4)_6(OH)_2$]. The slightly increased Ca/P ratio of HAp could be due to the carbonate substitution of the phosphate, which is in agreement with the FTIR results.

V. CONCLUSIONS

The results of our present biomimetic study (Table II) showed that the morphology and the size of apatite crystals in HAp nanocomposites were similar to the apatite present in the bone. Nanosized carbonated HAp with broad diffraction peaks is the main component of bone mineral[31,50] and was detected in our synthetic nanocomposites. In electron micrographs, the apatite in bone and in the synthetic nanocomposites appears as plate-like crystals with average dimensions of ~50 nm in length, ~25 nm in width, and 2–5 nm in thickness, and with strong preferred orientation in their c-crystallographic (002) axis. SAXS confirmed the formation of thin, elongated crystallites, whereas solid-state NMR proved the formation of nanocomposites. The inorganic content in the nanocomposites was much higher than in those synthesized without the hydroxyapatite-nucleating peptides,[19] but it is still lower than that found in natural bone.

In summary, we have successfully developed biomimetic polymer-hydroxyapatite nanocomposites using hydroxyapatite-nucleating peptides conjugated to self-assembling block copolymers. The thermoreversible gelation properties of these nanocomposites could potentially enable them to serve as injectable biomaterials for bone/cartilage tissue repair.

ACKNOWLEDGMENTS

This work was supported by the United States Department of Energy (DOE) Office of Basic Energy Services under Contract No. DE-AC02-07CH11358. This work benefited from the use of the APS and the IPNS, funded by the United States DOE, Office of Science, Office of Basic Energy Science under Contract No. DE-AC02-06CH11357.

REFERENCES

1. J. Aizenberg: Crystallization in patterns: A bio-inspired approach. *Adv. Mater.* **16,** 1295 (2004).
2. J.L. Arias, A. Neira-Carrillo, J.I. Arias, C. Escobar, M. Bodero, M. David, and M.S. Fernandez: Sulfated polymers in biological mineralization: A plausible source for bio-inspired engineering. *J. Mater. Chem.* **14,** 2154 (2004).
3. B.L. Smith, G.T. Paloczi, P.K. Hansma, and R.P. Levine: Discerning nature's mechanism for making complex biocomposite crystals. *J. Cryst. Growth* **211,** 116 (2000).
4. Z.Y. Tang, N.A. Kotov, S. Magonov, and B. Ozturk: Nanostructured artificial nacre. *Nat. Mater.* **2,** 413 (2003).
5. M. Aizawa, H. Ueno, K. Itatani, and I. Okada: Synthesis of calcium deficient apatite fibers by a homogeneous precipitation method and their characterization. *J. Eur. Ceram. Soc.* **26,** 501 (2006).
6. E.G. Bellomo and T. Deming: Monoliths of aligned silica-polypeptide hexagonal platelets. *JACS* **128,** 2276 (2006).
7. J.N. Cha, G.D. Stucky, D.E. Morse, and T.J. Deming: Biomimetic synthesis of ordered silica structures mediated by block copolypeptides. *Nature* **403,** 289 (2000).
8. G. Falini, M. Gazzano, and A. Ripamonti: Control of architectural assembly of octacalcium phosphate crystals in denatured collageneous matrices. *J. Mater. Chem.* **10,** 535 (2000).
9. J.L. Sumerel, W. Yang, D. Kisailus, J.C. Weaver, J.H. Choi, and D.E. Morse: Biocatalytically templated synthesis of titanium dioxide. *Chem. Mater.* **15,** 4804 (2003).
10. V. Bansal, D. Rautaray, A. Bharde, K. Ahire, A. Sanyal, A. Ahmad, and M. Sastry: Fungus mediated biosynthesis of silica and titania particles. *J. Mater. Chem.* **15,** 2583 (2005).
11. V.M. Rusu, C.H. Ng, M. Wilke, B. Tiersch, P. Fratzl, and M.G. Peter:

Size controlled hydroxyapatite nanoparticles as self-organized organic-inorganic composite materials. *Biomaterials* **26,** 5414 (2005).
12. J. Song, V. Malathong, and C.R. Bertozzi: A bottom-up approach for the development of artificial bone. *JACS* **127,** 3366 (2005).
13. J. Song, E. Saiz, and C.R. Bertozzi: An efficient process towards 3-dimensional bone-like composites. *JACS* **125,** 1236 (2003).
14. J. Song, E. Saiz, and C.R. Bertozzi: Preparation of PHEMA-CP composites with high interfacial adhesion via template driven mineralization. *J. Eur. Ceram. Soc.* **23,** 2905 (2003).
15. G. Xu, I. Aksay, and J.T. Groves: Continuous crystalline carbonate apatite thin films. *JACS* **123,** 2196 (2001).
16. D. Enlow, A. Rawal, M. Kanapathipillai, K. Schmidt-Rohr, S. Mallapragada, C.T. Lo, P. Thiyagarajan, and M. Akinc: Synthesis and characterization of self-assembled block copolymer templated calcium phosphate nanocomposite gels. *J. Mater. Chem.* **17,** 1570 (2007).
17. S. Chang, H. Chen, J. Liu, D. Wood, P. Bentley, and B. Clarkson: Synthesis of a potentially bioactive hydroxyapatite nucleating molecule. *Calcif. Tissue Int.* **78,** 55 (2006).
18. M. Determan, S. Seifert, P. Thiyagarajan, and S.K. Mallapragada: Synthesis and characterization of temperature and pH-sensitive self assembling pentablock copolymers. *Polymer (Guildf.)* **46,** 6933 (2005).
19. M. Kanapathipillai, Y. Yusufoglu, A. Rawal, Y-Y. Hu, C.T. Lo, P. Thiyagarajan, Y. Kalay, M.A. Akinc, S.K. Mallapragada, and K. Schmidt-Rohr: Ionic block copolymer template directed calcium phosphate nanocomposites. *Chem. Mater.* (2008) (in press).
20. J-F. Lutz, H.G. Boerner, and K. Weichenhan: Combining atom transfer radical polymerization and click chemistry: A versatile method for the preparation of end-functional polymers. *Macromol. Rapid Commun.* **26,** 514 (2005).
21. F. Zeng, H. Lee, and C. Allen: Epidermal growth factor-conjugated poly(ethylene glycol)-block- poly(d-valerolactone) copolymer micelles for targeted delivery of chemotherapeutics. *Bioconjugate Chem.* **17,** 399 (2006).
22. D. Bali, L. King, and S. Kim: Syntheses of new gramicidin a derivatives. *Aust. J. Chem.* **56,** 293 (2003).
23. V. Coessens, Y. Nakagawa, and K. Matyjaszewski: Synthesis of azido end-functionalized polyacrylates via atom-transfer radical polymerization. *Polym. Bull.* **40,** 135 (1998).
24. K. Schmidt-Rohr: Correlation of structure, mobility, and morphological information in heterogeneous polymer materials by two-dimensional wideline-seperation nmr spectroscopy. *Macromolecules* **25,** 3273 (1992).
25. J.C. Elliott: Studies in inorganic chemistry, in *Structure and Chemistry of the Apatites and Other Calcium Orthophosphates*, Vol. 18 (Elsevier, Amsterdam, The Netherlands, 1994), pp. 404.
26. S.V. Dorozhkin: Calcium orthophosphates. *J. Mater. Sci.* **42,** 1061 (2007).
27. Y. Yusufoglu and M. Akinc: Effect of pH on the carbonate incorporation into the hydroxyapatite prepared by an oxidative decomposition of calcium-edta chelate. *J. Am. Ceram. Soc.* **91,** 77 (2008).
28. M. Kumar, H. Dasarathy, and C. Riley: Electrodeposition of brushite coatings and their transformation to hydroxyapatite in aqueous solutions. *J. Biomed. Mater. Res.* **45,** 302 (1999).
29. R. Stulajterova and L. Medvecky: Effect of calcium ions on transformation brushite to hydroxyapatite in aqueous solutions. *Colloids Surf., A* **316,** 104 (2008).
30. S. Liao, F. Watari, M. Uo, S. Ohkawa, K. Tamura, W. Wang, and F. Cui: The preparation and characteristics of a carbonated hydroxyapatite/collagen composite at room temperature. *J. Biomed. Mater. Res. Part B: Appl. Biomaterials* **74,** 817 (2005).
31. M. Vallet-Regi and J.M. Gonzalez-Calbet: Calcium phosphates as substitution of bone tissues. *Prog. Solid State Chem.* **32,** 1 (2004).
32. S.A. Hutchens, R.S. Benson, B.R. Evans, H.M. O'Neill, and C.J. Rawn: Biomimetic synthesis of calcium-deficient hydroxyapatite in a natural hydrogel. *Biomaterials* **27,** 4661 (2006).
33. Z. Li, Y. Li, A. Yang, X. Peng, X. Wang, and Z. Xiang: Preparation and in vitro investigation of chitosan/nano-hydroxyapatite composite used as bone substitute materials. *J. Mater. Sci.-Mater. Med.* **16,** 213 (2005).
34. C. Lai, S. Tang, Y. Wang, and K. Wei: Formation of calcium phosphate nanoparticles in reverse microemulsions. *Mater. Lett.* **59,** 210 (2004).
35. E. Landi, G. Celotti, G. Logroscino, and A. Tampieri: Carbonated hydroxyapatite as bone substitute. *J. Eur. Ceram. Soc.* **23,** 2931 (2003).
36. J. Barralet, J.C. Knowles, S. Best, and W. Bonfield: Thermal decomposition of synthesized carbonate hydroxyapatite. *J. Mater. Sci.-Mater. Med.* **13,** 529 (2002).
37. B. Feng, J.Y. Chen, S.K. Qi, L. He, J.Z. Zhao, and X.D. Zhang: Carbonate apatite coating on titanium induced rapidly by precalcification. *Biomaterials* **23,** 173 (2001).
38. W.L. Murphy and D.J. Mooney: Bioinspired growth of crystalline carbonate apatite on biodegradable polymer substrata. *JACS* **124,** 1910 (2002).
39. K. Sato: Inorganic-organic interfacial interactions in hydroxyapatite mineralization processes. *Top. Curr. Chem.* **270,** 127 (2007).
40. S.V. Dorozhkin: In vitro mineralization of silicon containing calcium phosphate bioceramics. *JACS* **90,** 244 (2007).
41. I. Manjubala, S. Scheler, J. Bossert, and D. Jandt Klaus: Mineralisation of chitosan scaffolds with nano-apatite formation by double diffusion technique. *Acta Biomater.* **2,** 75 (2006).
42. J.P. Coates: The interpretation of infrared spectra: Published reference sources. *Appl. Spectrosc. Rev.* **31,** 179 (1996).
43. D.S.R. Krishna, A. Siddharthan, S.K. Seshadri, and T.S.S. Kumar: A novel route for synthesis of nanocrystalline hydroxyapatite from eggshell waste. *J. Mater. Sci.-Mater. Med.* **18,** 1735 (2007).
44. W.L. Suchanek, P. Shuk, K. Byrappa, R.E. Riman, K.S. TenHuisen, and V.F. Janas: Mechanochemical-hydrothermal synthesis of carbonated apatite powders at room temperature. *Biomaterials* **23,** 699 (2001).
45. D. Tadic and M. Epple: A thorough physicochemical characterisation of 14 calcium phosphate-based bone substitution materials in comparison to natural bone. *Biomaterials* **25,** 987 (2004).
46. W.P. Rothwell, J.S. Waugh, and J.P. Yesinowski: High-resolution variable-temperature phosphorus-31 NMR of solid calcium phosphates. *JACS* **102,** 2637 (1980).
47. J.P. Yesinowski and H. Eckert: Hydrogen environments in calcium phosphates: Proton MAS NMR at high spinning speeds. *JACS* **109,** 6274 (1987).
48. S.S. Hou, F.L. Beyer, and K. Schmidt-Rohr: High-sensitivity multinuclear nmr spectroscopy of a smectite clay and of clay-intercalated polymer. *Solid State Nucl. Magn. Reson.* **22,** 110 (2002).
49. P. Fratzl, N. Fratzl-Zelman, K. Klaushofer, G. Vogl, and K. Koller: Nucleation and growth of mineral crystals in bone studied by small-angle x-ray scattering. *Calcif. Tissue Int.* **48,** 407 (1991).
50. X. Su, K. Sun, F.Z. Cui, and W.J. Landis: Organization of apatite crystals in human woven bone. *Bone* **32,** 150 (2003).
51. M. Kikuchi, T. Ikoma, S. Itoh, H.N. Matsumoto, Y. Koyama, K. Takakuda, K. Shinomiya, and J. Tanaka: Biomimetic synthesis of bone-like nanocomposites using the self-organization mechanism of hydroxyapatite and collagen. *Compos. Sci. Technol.* **64,** 819 (2004).